Article

Cerium−Bismuth Oxides/Oxynitrates with Low Toxicity for the Removal and Degradation of Organophosphates and Bisphenols

Jiří Henych,* Martin Šťastný, Zuzana Němečková, Martin Kormunda, Zuzana Šanderová, Zuzana Žmudová, Petr Ryšánek, Štěpán Stehlík, Jakub Ederer, Michaela Liegertová, Josef Trögl, and Pavel Janoš

Read Online

ACCESS | Metrics & More | Article Recommendations | Supporting Information

ABSTRACT: Nanoscale cerium−bismuth oxides/oxynitrates were prepared by a scalable low-temperature method at ambient pressure using water as the sole solvent. Solid solutions were formed up to a 1:1 Ce/Bi molar ratio, while at higher doping levels, bismuth oxynitrate photocatalysts with a pronounced layered structure were formed. Bismuth caused significant changes in the structure and surface properties of nanoceria, such as the formation of defects, oxygen-containing surface groups, and Lewis and Brønsted acid sites. The prepared bifunctional adsorbents/photocatalysts were efficient in the removal of toxic organophosphate (methyl paraoxon) from water by reactive adsorption followed by photocatalytic decomposition of the parent compound and its degradation product (*p*-nitrophenol). Bi-doped ceria also effectively adsorbed and photodegraded the endocrine disruptors bisphenols A and S and outperformed pure ceria and the P25 photocatalyst in terms of efficiency, durability, and long-term stability. The very low toxicity of Bi-nanoceria to mammalian cells, aquatic organisms, and bacteria has been demonstrated by comprehensive in vivo/in vitro testing, which, in addition to its simple "green" synthesis, high activity, and durability, makes Bi-doped ceria promising for safe use in abatement of toxic chemicals.

KEYWORDS: nanoceria, bismuth, photocatalysis, reactive adsorption, paraoxon methyl, bisphenol S, bisphenol A

Adsorption/photodegradation on Bi-CeO₂ — BPS, BPA, MPO, BNPP
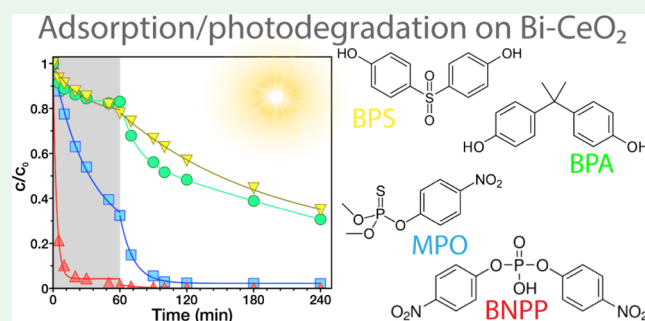
INTRODUCTION

Utilizing the extraordinary properties of various nanomaterials is a great opportunity to make progress in many environmental technologies, including water purification.[1] Their implementation may help to satisfy the growing demand for clean water, which is threatened by the growing number of so-called emerging pollutants.[2]

Contaminants of emerging concern[3] are typically non-regulated chemicals that comprise more than 40,000 chemicals,[4] including pharmaceuticals and personal care products; veterinary drugs and antibiotics; various nanomaterials; persistent organic pollutants, such as polybrominated flame retardants and perfluorinated compounds; endocrine-disrupting chemicals, represented by estrogens, androgens, and bisphenols; and some pesticides. Their concentration and acute toxicity may be relatively low, but the combined and long-term effects of this multitude of chemicals raise concern as they enter the environment and the food chain.

Nanostructured metal oxides (MOs) can be used as nanoadsorbents[5,6] and/or photocatalysts[7] as they are durable and inexpensive and are able to remove pollutants at very low concentrations and under varying conditions (such as pH and temperature). MOs are being investigated for abatement of heavy metals[8,9] and a wide variety of organic[10] and biological[11,12] pollutants. In addition to the most studied MO nanoadsorbents of iron,[13,14] titanium,[9,15] zinc,[16] and manganese,[17,18] cerium oxide is very popular because it is cheap and stable and has unique redox,[19] (photo)catalytic,[20] and multienzyme mimetic properties,[21] which can be effective against biological agents.[22]

In our previous works, we demonstrated the applicability of nanoceria for the adsorption and degradation of toxic organophosphorus (OP) pesticides[23] or chemical warfare agents,[24,25] or exploited its phosphatase-mimetic ability toward biologically relevant compounds.[26] In bifunctional TiO₂/CeO₂ nanocomposites,[25] accelerated decomposition of OP compounds was advantageously achieved by combining reactive adsorption with photoinduced degradation. CeO₂ reactivity is
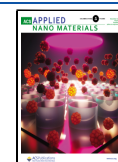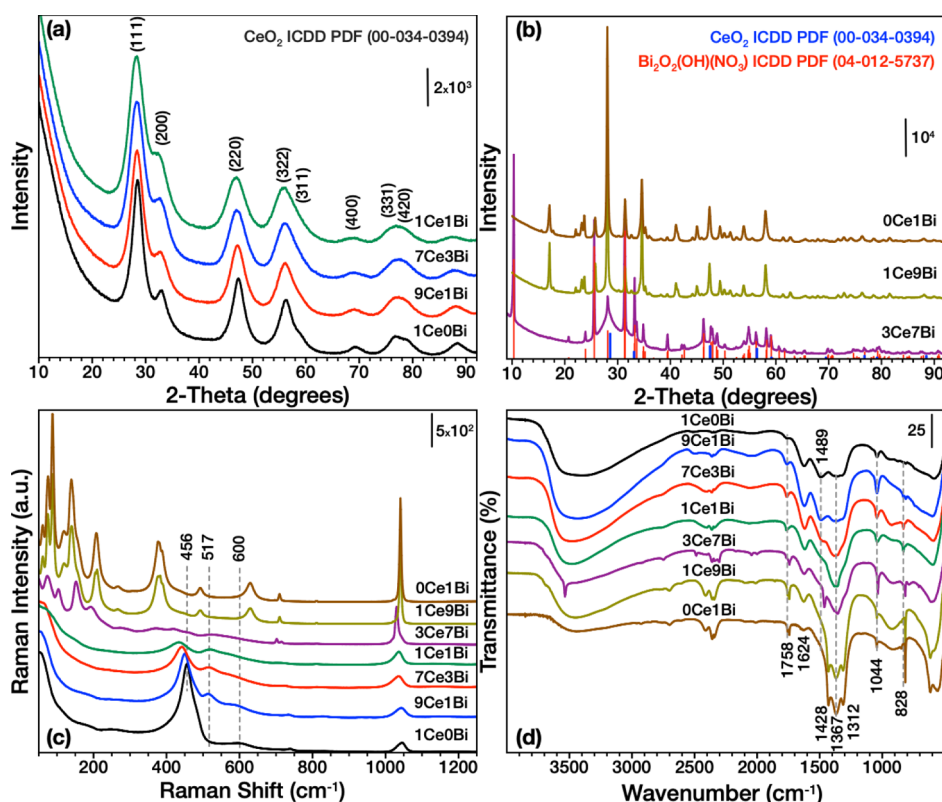
Figure 1. X-ray diffractograms of prepared (a) Ce−Bi oxides and (b) ceria/bismuth oxynitrates and Raman (c) and FTIR (d) spectra of all prepared samples.

ascribed to the easy change of Ce^{3+}/Ce^{4+} states, high oxygen mobility, and surface defect structure,[27,28] which can be controlled by the synthesis method or created by doping or temperature treatment in various atmospheres.

Combining nanoceria with bismuth compounds, which are often also photocatalytic, cheap, and have low toxicity,[29] can be particularly useful. Bi doping can improve the mobility of lattice oxygen by decreasing the formation energy of oxygen vacancies (OVs) and weakening the Ce−O bond, as demonstrated both theoretically[30] and experimentally.[30,31] In addition, unique asymmetrical vacancy sites formed in Bi/ceria[32] allow for easy attachment and release of oxygen, which may be particularly useful for catalytic reactions. Bi-modified ceria can be prepared hydrothermally[33,34] in an autoclave, which can be difficult for up-scaling, or by coprecipitation[30,31] followed by calcination (500 °C[31] or 600 °C[30]), which requires high energy consumption and results in larger, less reactive particles, or the sol−gel method[35] using organic solvents and high-temperature annealing (700 °C).

Herein, nanocrystalline cerium−bismuth oxides/oxynitrates were prepared by an easily scalable low-temperature (up to 100 °C) method at ambient pressure using only common chemicals and water as the only solvent. We showed that bismuth causes significant changes in the structure and surface properties of nanoceria, which leads to substantially enhanced adsorption and photocatalytic activity. Several model compounds were used for this study, namely OP compounds (i) methyl paraoxon (MPO)—active metabolite of the OP pesticide methyl parathion and (ii) bis(*p*-nitrophenyl)-phosphate (BNPP)—an artificial substrate used for evaluating phosphatase-like enzyme activity and endocrine disrupting compounds (iii) bisphenol A (BPA) and (iv) bisphenol S

(BPS). Finally, the toxicity of selected CeO_2-based materials was evaluated in several standardized tests to assess their impact on aquatic (and other) organisms.

MATERIALS AND METHODS

Sample Synthesis. A series of Ce/Bi oxides with different molar ratios (1:0, 9:1, 7:3, 1:1, 3:7, 1:9, and 0:1; samples denoted accordingly as XCeYBi) was prepared by wet chemical precipitation and refluxing in water at ambient pressure and low temperature (<100 °C) without any calcination, following the procedure reported elsewhere.[36] See the detailed procedure in the Supporting Information.

Characterization Methods. XRD, X-ray fluorescence (XRF), XPS, electron microscopy (SEM and TEM) with EDS, spectroscopy (UV−vis, Raman, and FTIR), nitrogen physisorption, acid−base titrations, and zeta potential measurements were used to characterize the materials. See details in the Supporting Information.

Degradation of Pollutants. OP compounds, MPO and BNPP, and endocrine-disrupting compounds, BPA and BPS, were selected as model pollutants for the degradation tests. The compounds were removed from water by a combination of (reactive) adsorption (in the dark) and photo-induced degradation (PID). See measurement details in the Supporting Information.

To elucidate the role of reactive oxygen species (ROS) in photocatalytic decomposition, a series of trapping experiments (on sample 1Ce1Bi) was conducted using different ROS scavengers. Isopropanol (IPA), ethylenediaminetetraacetic acid disodium salt (EDTA-2Na), and ascorbic acid (AA) at a concentration level of 1 mmol·L^{-1} were used to scavenge hydroxyl radicals ($^{\bullet}OH$), holes (h_{vb}^{+}), and superoxide ion radicals ($O_2^{\bullet-}$), respectively.

In Vivo/In Vitro Toxicity Testing. The environmental toxicity of the materials was assessed using representative organisms at all stages of the food chain, that is, primary producers (algae), consumers (fish and invertebrates), and destruents (bacteria). Algal toxicity was assessed in accordance with ISO 8692:2012 using the alga
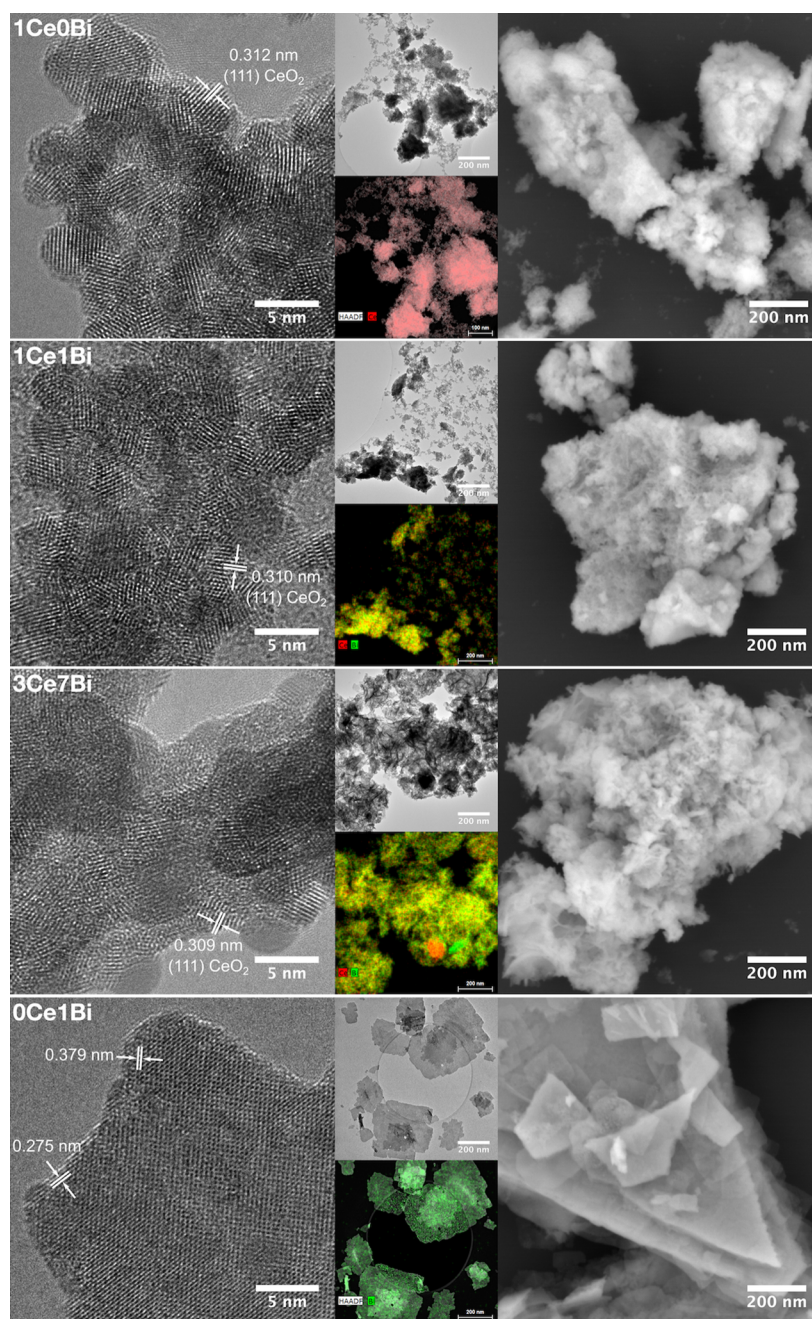
Figure 2. HRTEM (left), TEM/EDS (center), and SEM (right) analyses of the selected Ce–Bi samples.

Desmodesmus quadricauda, while bacterial toxicity was determined by a growth test using *Escherichia coli*, *Staphylococcus aureus*, and *Rhodococcus erythropolis*, representing Proteobacteria, Firmicutes, and Actinobacteria, respectively. See detailed procedures in the Supporting Information. Toxicity to the brine shrimp *Artemia salina* was determined according to the procedure described previously.[37]

In Vitro rMSC PrestoBlue Cytotoxicity Assay. Rat bone marrow mesenchymal stem cells (*Rattus norvegicus*, Sigma-Aldrich Inc.) were used to evaluate in vitro cytotoxicity to mammalian cells, as described in detail in the Supporting Information. The cytotoxicity assay was performed using six concentrations (0.001, 0.01, 0.1, 1, 10, and 100 μM) of the 1Ce0Bi and 1Ce1Bi samples and controls (positive control: 5% hydrogen peroxide; negative control: sample free media). Cytotoxic effects were determined after 96 h by the PrestoBlue (ThermoFisher Scientific, A13261) assay.

Fish Embryo Test. The fish embryo test (FET) using zebrafish *Danio rerio* was performed at six concentrations (0.001, 0.01, 0.1, 1,

10, and 100 μM) of the 1Ce0Bi and 1Ce1Bi samples and controls (positive control: 4 mg/L of dichloroaniline; negative control: ISO water) for 96 h at 26.9 ± 1 °C. 24 embryos per concentration or control was used as individual replicates. See ref 38 and Supporting Information for details.

■ RESULTS AND DISCUSSION

Characterization of $Ce_{1-x}Bi_xO_y$ Solid Solutions. As shown previously,[36] small (<5 nm) but highly crystalline aggregated ceria nanoparticles with a unique defect structure were formed by simple refluxing of cerium hydroxide precipitated in water and treated with H_2O_2, as evidenced by XRD (Figure 1a, Table S1), Raman spectroscopy (Figure 1c), electron microscopy with EDS analysis (Figures 2, S1–S3, Table S2), and XPS (Table S3, Figure S4). However, since the samples were prepared at a relatively low temperature,

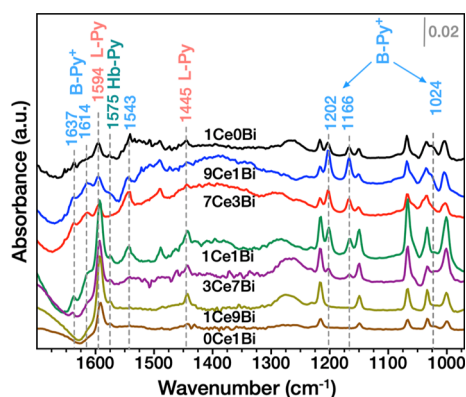**Figure 3.** DRIFTS spectra of pyridine adsorption on prepared Ce−Bi samples.

Scheme 1. Proposed Overall Reaction Mechanism for the Dissociative Adsorption and Photocatalytic Degradation of MPO

nanoceria can contain some amount of residual hydrous oxide $CeO_2 \cdot 2H_2O$, indiscernible from CeO_2 by XRD. XRD analysis showed that the cubic ceria structure as a single phase was
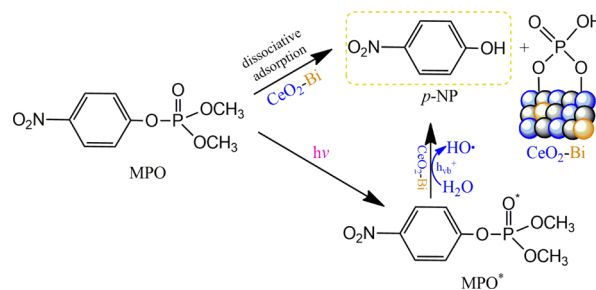
preserved even after bismuth doping up to a 1:1 Ce/Bi molar ratio (Figure 1a). Nevertheless, bismuth doping induced significant structural changes, such as linear lattice expansion with a concomitant reduction in crystallite size from 3.2 nm for pure nanoceria down to 2 nm for the 1Ce1Bi sample (Table
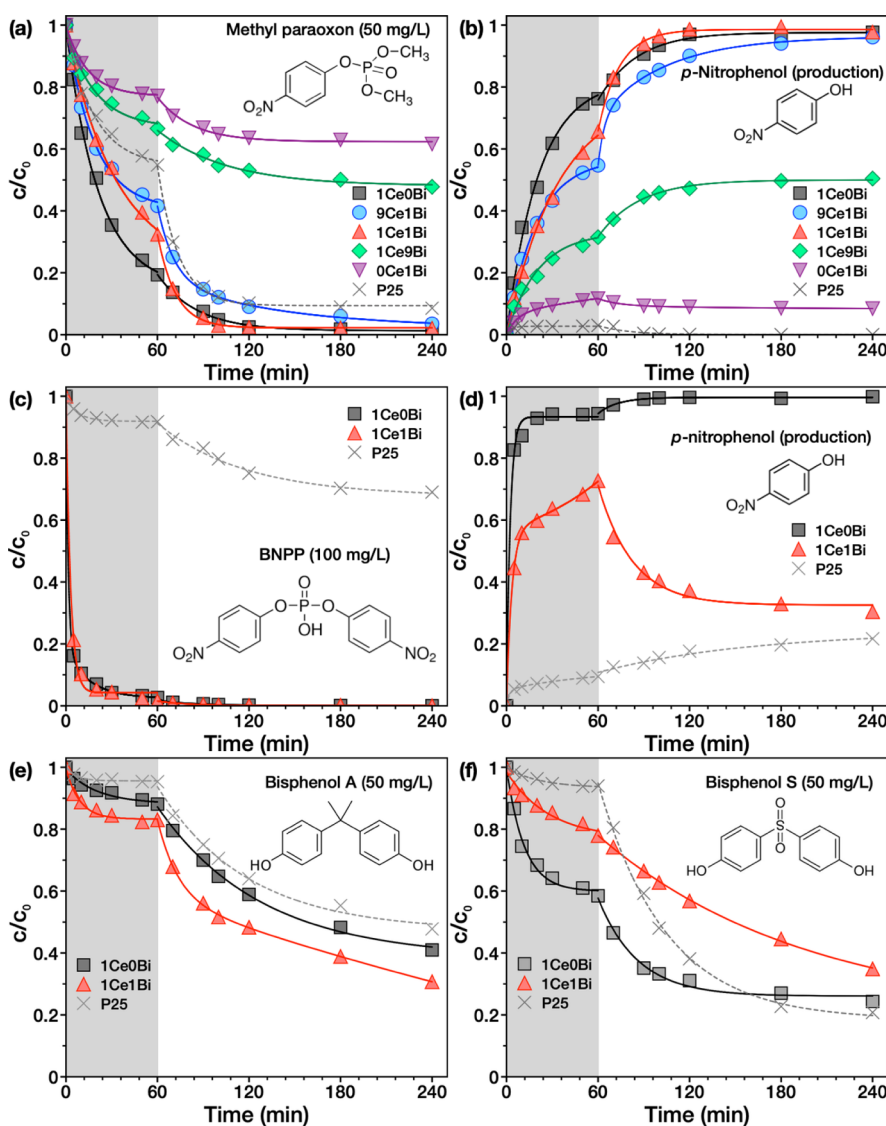

Figure 4. Degradation kinetic curves for reactive adsorption and PID of (a) MPO with concomitant production of its degradation product *p*-nitrophenol (b); (c) BNPP with its product *p*-nitrophenol (d); and adsorption and PID of bisphenols A (e) and S (f) on selected Ce/Bi oxides in comparison with P25 (TiO_2) as a benchmark photocatalyst.
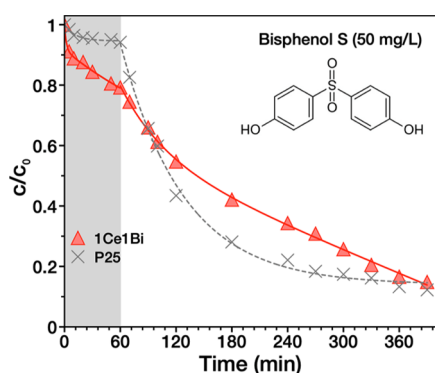
Figure 5. Long-term experiment (390 min) of photo-induced degradation of BPS using the 1Ce1Bi sample in comparison with the P25 benchmark photocatalyst.

S1). As reported in previous works,[31,39] successful structural Bi doping of ceria crystal structure led to lattice expansion, as Bi^{3+} has a larger cation radius (1.17 Å) than Ce^{4+} (0.97 Å), the size of the coherent domain decreased, and OVs were formed. These are consistent with our study (see lattice parameters and size of the crystallites presented in Table S1), and it indicates that structural Bi doping can be achieved by soft water-based synthesis. The analysis of d-spacing (Figures 2 and S1−S3) was consistent with XRD results. The value ~0.31 nm found in all samples up to the 1:1 Ce/Bi ratio corresponded well to the (111) plane of CeO_2.

Structural changes can also be observed in the Raman spectra (Figure 1c). The main CeO_2 symmetric breathing vibration band (F_{2g}) was found to be broadened significantly, decreased in intensity, and downshifted from 456 cm^{-1} for pure ceria (1Ce0Bi) to 437 cm^{-1} for 1Ce1Bi. These changes

were caused by a disorder in the oxygen sublattice, which is related to the decreasing particle size and lattice expansion and due to charge-compensating defects induced by doping of Bi^{3+} cations into the CeO_2 lattice.[31] It has been previously reported[33] that the cubic structure of ceria can accommodate relatively large amounts of foreign Bi^{3+} cations with a lower valence than Ce^{4+} to form a solid solution of $Ce_{1-x}Bi_xO_y$, where x can vary between 0.2 and 0.6, strongly depending on the preparation method. As demonstrated here, ceria doping with a relatively high amount of bismuth (up to 0.5) can be achieved by a soft water-based method without hydrothermal treatment.

Furthermore, the broad band at 1037 cm^{-1} in Raman spectra assigned to residual nitrates from the synthesis retained its low intensity up to the 1:1 Ce/Bi ratio, but it shifted and became sharp and intense at higher Bi concentrations as new phases of bismuth oxynitrates formed (discussed below). The new bands at 517 and 600 cm^{-1}, which both became prominent upon Bi doping (up to 1Ce1Bi), can be ascribed to the presence of Bi^{3+} ions and the formation of charge-compensating OVs, respectively.[31,40] Vacancy formation leads to an increase in optical absorption and a reduction of the band gap energy (E_{bg}) by introducing shallow bands,[41] as evidenced by Tauc plots derived from UV−vis reflectance spectra for direct and indirect transitions (Figure S5), which show that E_{bg} for direct transition decreased from 2.83 eV for pure ceria to 2.48 eV for 1Ce1Bi. The disorder induced by Bi doping can facilitate the dissociative adsorption of dioxygen and water, which is more favorable on the defective ceria surface[42,43] and can lead to the formation of various oxygen-containing surface species, for example, surface hydroxyl groups. Indeed, a higher number of surface −OH groups on CeO_2−Bi samples up to a 1:1 Ce/Bi ratio was detected by
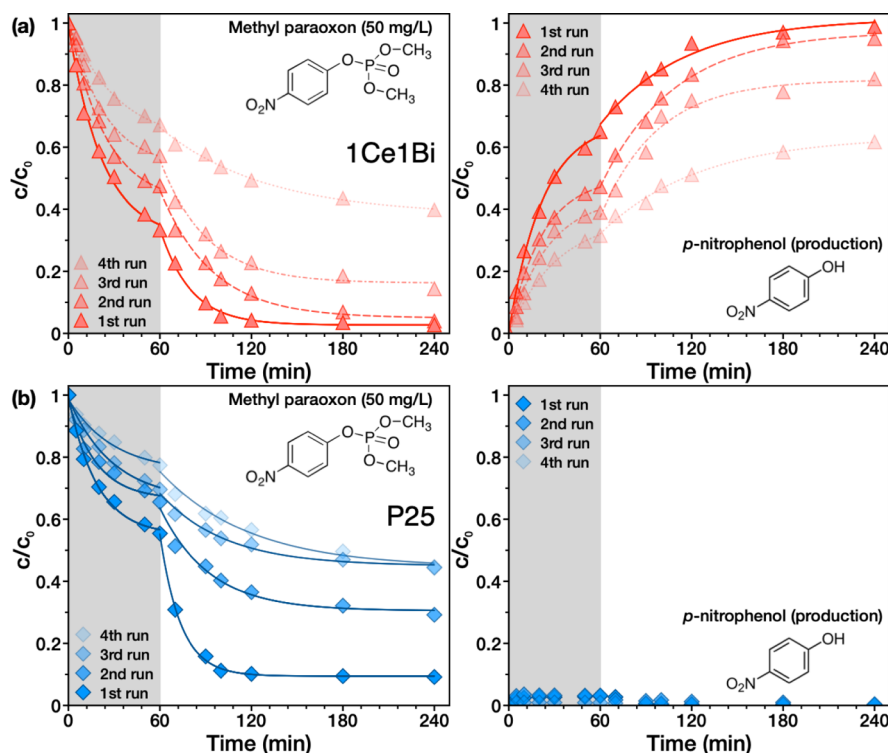

Figure 6. Recycling experiment of the photocatalytic decomposition of MPO (left) with the concomitant production of p-NP (right) on the sample 1Ce1Bi (a) and P25 (b).
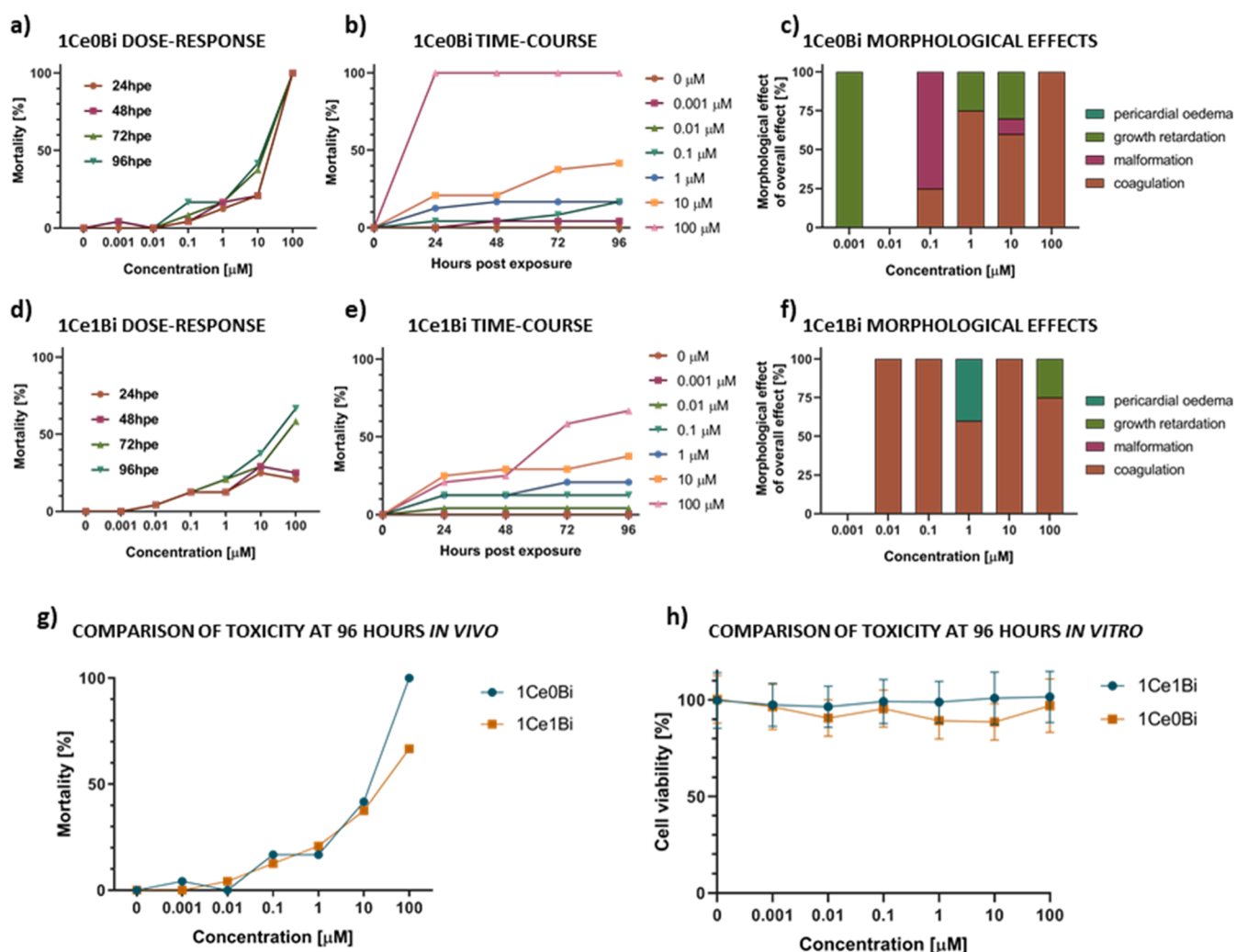
Figure 7. In vivo/in vitro toxicity assays. (a−g) FET results for various concentrations of 1Ce0Bi and 1Ce1Bi. (a,b,d,e) Dose−response and time-course development curves of the tested concentrations of 1Ce0Bi and 1Ce1Bi; (g) comparison of the in vivo toxicity of 1Ce0Bi and 1Ce1Bi. (c,f) Morphological effects caused by the exposure to individual concentrations over the whole 96 h period. Note: The absence of error bars means a single FET experiment with 24 embryos per concentration as individual replicates. (h) Comparison of the in vitro toxicity (cytotoxicity) of 1Ce0Bi and 1Ce1Bi on the rMSC cell line.

FTIR spectroscopy (Figure 1d), as well as by XPS (Figure S4, Table S3) and acid−base titrations (Table S4), which will be discussed further below. In the FTIR spectra, a broad band centered at about 3440 cm^{-1} together with a band at 1624 cm^{-1} belong to the adsorbed water and surface hydroxyl groups, respectively. The gradual increase of the bands between 1500 and 1300 cm^{-1}, which became prominent at a higher Bi content, clearly shows the presence of NO_3^-.

Only one phase and morphology of the aggregated nanoparticles (Figures 2, S1 and S2) was preserved up to a 1:1 Ce/Bi molar ratio but with an apparent merging of individual nanoparticles at higher doping levels. Bi doping also caused a gradual decrease in the surface area and pore volume of nanoceria (Table S1).

Ceria/Bismuth Oxynitrates. At a Ce/Bi molar ratio higher than 1:1, in addition to CeO_2, a new bismuth-containing phase was formed. In the sample 3Ce7Bi, the basic oxynitrate $Bi_2O_2(OH)(NO_3)$ forming a flower-like nanocomposite with CeO_2 (Figure 2) was identified in XRD patterns (Figure 1b), while in samples 1Ce9Bi (Figure S3) and 0Ce1Bi (Figure 2), a new unidentified highly crystalline phase

with a distinct layered structure was formed. Basic bismuth oxynitrates (BiON) resulting from the hydrolysis or thermal dehydration of bismuth nitrate pentahydrate exhibit rich crystal chemistry with many complicated compositions.[44] The unknown phase was therefore attributed to some other type of BiON, but we did not find this structure in previous works,[44−47] including the references in this review.[48] Several BiONs are efficient photocatalysts for the degradation of contaminants.[45,46,48] The layered structure comprises $[Bi_2O_2]^{2+}$ layers with embedded OH^- and $(NO_3)^-$ groups, which induce spontaneous polarization and effectively separate photogenerated charge carriers.[45] The preparation of BiON with well-defined compositions through a facile route is still a challenge. As shown here, these structures can be easily prepared by refluxing bismuth nitrate aqueous solutions instead of the hydrothermal route.

The bands at 76, 104, 153, and 194 cm^{-1} in the Raman spectrum of 3Ce7Bi (Figure 1c) correspond well to the $Bi_2O_2(OH)(NO_3)$ phase.[49] The spectra of 1Ce9Bi and 0Ce1Bi show very rich spectral features, which are typical of bismuth oxides at 62, 77, 89, 119, 139, 159, 207, 268, 380

(combination), 493, and 629 cm^{-1}. In general, vibrations in the 100−200 cm^{-1} region belong to the Bi^{3+}−O vibrations in BiO$_6$ octahedra, and those between 120 and 150 cm^{-1} may be assigned to the displacement of bismuth and oxygen atoms, while BiO$_6$ octahedral units have vibrations between 600 and 1000 cm^{-1}.[50−52] Most bands up to 300 cm^{-1} are similar to α-Bi$_2$O$_3$, where the mode 119 cm^{-1} comes from the A$_g$ symmetry and the modes 139 and 159 cm^{-1} are related to the displacements of both Bi and O atoms.[50] The complex combination of bands at 380 and 493 cm^{-1} is related to O−Bi−O or Bi−OH bonds,[53−55] and the 629 cm^{-1} mode can be attributed to the Bi−O vibration of non-bridging oxygen,[55] while the 709 cm^{-1} mode and very strong 1041 cm^{-1} mode are features of NO$_3^-$,[45] which altogether indicate some type of BiON of unidentified structure produced by dehydration reactions under thermal treatment with reflux. While for CeO$_2$ (and Bi-doped ceria), the residual free nitrates from the synthesis lead to a broad small peak at 1037 cm^{-1}, the formation of a distinct layered structure in BiON (3Ce7Bi) comprising [Bi$_2$O$_2$]$^{2+}$ layers with embedded OH$^-$ and (NO$_3$)$^-$ groups probably results in different polarizations and a red shift of this band to 1031 cm^{-1}. At even higher Bi amounts (1Ce9Bi and 0Ce1Bi), this band becomes very sharp and intense.

Accordingly, in the FTIR spectra of 1Ce9Bi and 0Ce1Bi (Figure 1d), the bands at 617 and 559 cm^{-1} belong to the Bi−O stretching modes.[56] The bands at 828 and 1041 cm^{-1} of nitrates[57] in Ce$_{1-x}$Bi$_x$O$_{2-\delta}$ solid solutions (up to a 1:1 Ce/Bi ratio) become very sharp and narrow at a higher Bi concentration when BiON phases are formed.

Along with the formation of a new phase, the morphology of the samples changed dramatically. In the 3Ce7Bi sample (Figure 2), flower-like aggregates of Bi$_2$O$_2$(OH)(NO$_3$) with a size of a few microns formed, similar to those prepared hydrothermally by Han et al.,[45] with highly dispersed but firmly attached nanoceria particles. Their formation was also confirmed by d-spacing analysis (Figure 2), the found value of 0.309 nm was assigned to the (111) plane of CeO$_2$. The samples 1Ce9Bi (Figure S3) and 0Ce1Bi (Figure 2) have a distinct layered structure, which consists of thin stacked highly crystalline (see TEM in Figure 2 on the left) sheets with a size of several hundred nanometers, typical of BiON with a Sillén/Aurivillius-type[58] structure. Detailed TEM and SEM analysis of the 1Ce9Bi sample (Figure S3) revealed the presence of dispersed nanoparticles on the nanosheets. Elemental analysis by EDS (Figure S3 inset) showed a higher amount of cerium in the particles, and the d-spacing of the particles corresponds to the (111) plane in CeO$_2$, suggesting the formation of dispersed nanoceria on the sheets, although they were not identified by XRD or Raman spectroscopy, probably due to the low amount of very small and highly dispersed particles. The additional d-spacing values of ∼0.38 and ∼0.28 nm of an unidentified layered structure were found in samples 1Ce9Bi and 0CeBi.

Elemental Composition and Surface Chemical Properties. Samples' bulk composition was studied by XRF and TEM/EDS (Table S2), while the surface composition was investigated by XPS (Figure S4, Table S3). Surface chemical properties were evaluated by acid−base (Table S4) and zeta potential titrations (Figure S6) and pyridine adsorption (Figure 3).

Bi, Ce, O, and C were detected on the surface layer of the samples by XPS, while only traces (up to 3 at. %) of nitrogen were detected in BiONs. Note that the XPS sensitivity for nitrogen is low. The high-resolution spectrum of Bi 4f (Figure S4) shows two signals at 158.4 and 163.7 eV, corresponding well to Bi 4f$_{7/2}$ and Bi 4f$_{5/2}$ of Bi^{3+} in all samples.[59] Complex Ce states were assigned according to a previous work.[60] In all samples, predominantly Ce^{4+} states with the contribution of reduced Ce$^{<4+}$ states (ranging between 7 and 17%) were found, which is typical for nanoceria prepared by the wet chemical method. The O 1s peak is quite complex due to a number of various expected species and was fitted tentatively by four components—Ce^{4+}−O (529.6 eV, red), Ce$^{<4+}$−O (531.6 eV, ocher), Bi^{3+}−O (529.5 eV, blue), and X−OH (X = Ce, Bi; 532.7 eV, green). The surface chemical composition (Table S3) clearly shows a lower Ce/Bi ratio on the surface than the theoretical and in the bulk (see EDS and XRF analyses data in Table S2), indicating that Bi is distributed mainly on the surface of the samples. The elemental compositions obtained by EDS and XRF are in relatively good agreement.

The number of surface hydroxyl groups (q_{OH}, Table S4), which also strongly affects the surface charge of the materials in solution, can be calculated from acid−base titration curves.[61] The surface hydroxyl site density (α_{OH}), obtained by normalizing q_{OH} per surface area, increases with increasing amount of Bi in the sample. Measurement of the zeta potential as a function of pH (Figure S6) shows that all samples have highly positive values (above +30 mV) at pH 4−8, which indicates very good colloidal stability of the particles in aqueous solutions. Moreover, increasing Bi concentration in the samples significantly (i) increases their positive zeta potential (by about +5−8 mV), which further improves colloidal stability in solution at higher pH values (by 1−2) and (ii) increases the isoelectric point (pH$_{iep}$) from 9.3 for pure ceria to the highest value of 11.8 for the 1Ce9Bi sample due to the increased formation of OVs[43] and the higher number of basic surface groups. This is in accordance with XPS and acid−base titrations, which also show a significant change in the surface chemical properties of Bi-modified samples.

Adsorption of gaseous pyridine (Py) on the solid surface can provide information on surface acid sites (Figure 3). In the spectra of all samples, the band at about 1594 cm^{-1} together with the combination band at 1444 cm^{-1} results from coordination of Py to unsaturated metal cations representing Lewis acid sites (L-py).[62,63] Interestingly, its intensity is higher for Bi-modified samples (especially for 1Ce1Bi), indicating a higher number of acid sites, probably because Bi cations are predominantly distributed (and exposed) on the surface (see XPS results). Furthermore, the gradual shift of the 1594 cm^{-1} band to lower values at higher Bi concentrations suggests a slightly lower acidity of the metal sites due to the substitution of Ce by Bi cations. The small band at about 1575 cm^{-1} visible in all samples results from hydrogen-bonded Py to weakly acidic isolated surface OH groups (Hb-Py).[62,63] Interestingly, the bands at 1637, 1614, 1202, and 1166 cm^{-1} indicate the presence of H-donor sites with Brønsted acidity by forming pyridinium ions.[62−64] The formation of these sites is related to the synthesis procedure utilizing hydrogen peroxide, which causes the formation of a highly defective structure with various oxygen-containing surface species (such as OH groups), which is not typical for ceria prepared by other wet chemical methods, as shown in our previous work.[36] The formation of H-donor sites may also be related to surface hydroxyl groups from residual Ce(OH)$_4$ in samples prepared at low temperature and OH groups in the BiON structure (3Ce7Bi). As is evident, Bi doping increases Brønsted acidity

(up to 1Ce1Bi), while these sites are diminished in basic oxynitrates. In general, the 1Ce1Bi sample shows the largest number of both Lewis and Brønsted acid sites.

Degradation of OP Compounds. The prepared Ce−Bi samples were used for degradation of OP compounds MPO and BNPP by the combined effects of reactive adsorption and UV-induced photodecomposition (for clarity, only selected samples are presented in Figure 4a−d, and kinetic parameters, including rate constants, for all samples are given in Tables S5 and S6). MPO is a highly toxic active metabolite of the methyl parathion herbicide, which is readily soluble in water and is also often used as a simulant of GB and VX chemical warfare agents.[65] BNPP is structurally similar to some OP pesticides, is soluble in water, and is used as a model compound to estimate phosphodiesterase (PED) activity.[66]

Consistent with our previous work,[25] pure nanoceria (Figure 4a, black squares) prepared by peroxo-route has a good ability to degrade OP compounds (such as MPO) in the dark by dissociative adsorption to form p-nitrophenol (p-NP) as its degradation product (Figure 4b) by the S_N2 nucleophilic substitution mechanism. Bi-doped ceria samples show a slightly lower initial adsorption/degradation rate than MPO, while BiONs show a significant decrease of both adsorption and degradation activity, likely due to the significantly reduced surface area and changes in surface properties. The P25 photocatalyst used here as a benchmark shows relatively good adsorption capacity (but still lower compared to Bi-doped ceria), but is unable to degrade MPO, which is consistent with our previous observations,[26] indicating low or no TiO_2 reactivity toward OP pesticides.

UV illumination (from 60 min onward) initiates/accelerates the degradation of MPO on all samples (including BiONs), proving that they all act as photocatalysts. As expected, P25 exhibits a high rate of PID, but after 120 min, the residual MPO concentration does not decrease further, probably due to the accumulation and preferential degradation of slowly degrading products. Interestingly, no p-NP production was observed in solution. In contrast, pure ceria and Bi-doped samples degrade all MPO in solution with the concomitant build up of p-NP as the main degradation product. This suggests that the degradation mechanism on P25 may be different compared to nanoceria, or that the p-NP produced on P25 is not released into solution but rather degrades further on its surface.

The selected samples (pure ceria, P25, and 1Ce1Bi) were used to degrade another OP compound, BNPP (Figure 4c,d, Tables S7 and S8), which can be used to estimate PED activity. BNPP is more prone to spontaneous degradation compared to MPO; therefore, twice higher initial concentration was used. Nanoceria and the 1Ce1Bi sample rapidly degrade all BNPP within minutes in the dark, proving their excellent PED activity, while P25 has only negligible reactivity. Nevertheless, as can be seen, pure ceria produces a higher amount of p-NP compared to 1Ce1Bi (Figure 4d), which proves that substitution of Ce cations by Bi is slightly detrimental to PED activity due to different acid−base properties of the cationic centers.

UV illumination initiates the slow degradation of BNPP on the P25 catalyst with concomitant p-NP production, but the BNPP concentration remained above 70% after 240 min, indicating a relatively low ability of P25 to degrade it. As with P25, UV light accelerates the production of p-NP on pure nanoceria, whose concentration remains constant after 120

min. In stark contrast, on 1Ce1Bi, UV illumination leads to rapid degradation of p-NP, indicating a much better ability of Bi-doped ceria to degrade parent OP compounds (such as BNPP) along with its degradation product (p-NP) compared to pure ceria and P25 photocatalysts. To demonstrate this, the samples were tested for PID of p-NP alone (Figure S7). As is evident, 1Ce1Bi significantly outperforms all other samples in p-NP adsorption and photodecomposition, indicating its suitable surface properties for p-NP adsorption and a high photocatalytic activity due to Bi doping.

The improved photocatalytic performance of the 1Ce1Bi sample can be caused by several effects. In addition to the change in surface and adsorption properties, Bi doping causes disorders and defects in the ceria structure (see Raman and XPS results) that can act as trapping sites for excited electrons and holes, which can lead to their better separation and thus restrict their recombination.[67] Moreover, Bi doping decreased the band gap (Figure S5), which should lead to easier (faster) excitation of the electrons that can be trapped on the defects and disorders caused by Bi doping.[34] These effects should contribute to improved photocatalytic decomposition.

Trapping Experiment of the Photogenerated Active Species. The reactive species generated during the MPO photodegradation on the 1Ce1Bi sample were identified by free radical and hole trapping experiments in the presence of various scavengers in the reaction solution, including IPA (for $^{\bullet}OH$ scavenger), EDTA-2Na (h_{vb}^+), and AA ($O_2^{\bullet-}$) (Figure S8). Without any scavenger, ca. 35% of MPO was photodegraded upon illumination (at time 240 min). When IPA was added to the reaction solution and illuminated, the efficiency of photodegradation was reduced to only ∼6%, while it was reduced to 9% in the presence of EDTA. The addition of AA to the reaction leads to a slight decrease of the photocatalytic efficiency to ca. 27%. This indicates that the hydroxyl radicals ($^{\bullet}OH$) are the primary active species for MPO decomposition together with photogenerated holes (h_{vb}^+), and $O_2^{\bullet-}$ radicals contribute only a little to the photodegradation. These results seem to be consistent with our investigations of Bi-doped ceria. The defects, such as OVs that are readily formed upon Bi doping can boost the separation of photogenerated charge carriers (electron−hole pairs) and therefore (h_{vb}^+) can significantly participate in photodegradation. Moreover, the formation of the ($^{\bullet}OH$) radical, which significantly contributes to photodegradation, is also very favorable due to the large number of oxygen-containing surface groups and adsorbed water (see XPS and FTIR results) on the sample 1Ce1Bi, which is related to defect formation or water-based synthesis.

MPO Degradation Mechanism. The MPO degradation can be thus described by several consecutive steps as follows: (i) The dissociative adsorption (in the dark) is realized through the binding of the phosphoryl oxygen in the MPO molecule to the metal cation on the CeO_2−Bi surface. Then, a surface hydroxyl group attacks the central P atom, resulting in the production of p-nitrophenol (p-NP) as a leaving group by S_N2 nucleophilic substitution. At the same time, the residual phosphate can be bound to the surface of the catalyst. (ii) Upon light irradiation, generated positive holes (h_{vb}^+) react directly with MPO or with adsorbed water (H_2O_{ads}) or surface hydroxyl groups to give strong oxidizing $^{\bullet}OH$ radicals at the MO surface according to eq 1

$$H_2O_{ads} + h_{vb}^+ \rightarrow {}^{\bullet}OH + H^+ \tag{1}$$
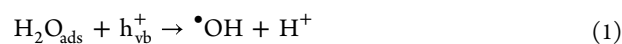
The $^{\bullet}$OH radicals immediately react with the MPO molecule to form its excited intermediate (MPO*), which accelerates its further degradation to the main degradation product p-nitrophenol (p-NP). This mechanism is proposed in Scheme 1.

Degradation of BPA and BPS. The selected samples were further tested for PID of endocrine disruptors BPA and BPS (Figure 4e,f, Table S9), which are not spontaneously degraded in the dark by reactive adsorption on nanoceria. As is evident, the adsorption of bisphenols is very different on P25, ceria, and Bi-modified sample (1Ce1Bi) and is strongly dependent on the surface structure of the catalyst (and acid−base properties) and the bisphenol structure.

The sample 1Ce1Bi shows the highest affinity to BPA (17% of BPA pre-adsorbed), followed by pure ceria (12%), and the lowest adsorption was observed on P25 (<5%). Interestingly, this order was maintained also for PID of BPA (initiated at t = 60 min), as indicated by the rate constants (Table S9). This demonstrates that a good match between the adsorbate and the adsorbent plays a major role for its further photodecomposition.

BPS has a different structure containing a sulfonyl group, is more hydrophilic than BPA, and has a higher dipole moment,[68] which all result in very different adsorption properties. Again, on P25, the amount of preadsorbed BPS during 60 min in the dark was negligible (6%), while 1Ce1Bi showed almost four times better adsorption (22%), and that of pure ceria was almost seven times better (42%). The superior adsorption of BPS on nanoceria may be due to the high affinity of the oxygen in the sulfonyl group for the ceria surface (analogous to the phosphonyl group). As is evident, Bi doping alters the surface chemical properties of the catalyst, which results in different adsorption of pollutants. The sample 1Ce1Bi with more acidic surface Ce^{4+} cations replaced by Bi^{3+} (with higher basicity, see Table S4) and with substantially higher number of surface hydroxyl groups (as shown by XPS) and different surface acid sites (Figure 3) shows slightly better BPA adsorption but lower BPS adsorption compared to pure nanoceria. This indicates that the sulfonyl group in the pollutant structure promotes adsorption onto nanoceria and that the selectivity of the catalyst (toward BPA or BPS) can be controlled to some extent by replacing Ce cations with Bi cations.

Nevertheless, P25 shows the highest initial PID rate (and thus the highest total removal rate after 240 min−79%) followed by pure ceria (76%) and 1Ce1Bi (65%). However, the degradation kinetics are very different for each sample. As is evident, PID utilizing P25 is very rapid at first but slows down at a later stage as some difficult-to-degrade intermediates are formed. Pure ceria shows a similar course of reaction. In contrast, the 1Ce1Bi sample shows a lower initial rate but without a significant slowdown of the reaction at longer illumination times. Therefore, P25 and 1Ce1Bi were tested in a prolonged degradation experiment (Figure 5), which indicates that the 1Ce1Bi sample will outperform P25 at longer times (>390 min). This suggests that the adsorbent surface structure has a tremendous effect on the degradation of BPS. Here, P25 (and pure ceria) produces some intermediates that hinder degradation of the parent compound (BPS) at longer times, while on 1Ce1Bi the mechanism of degradation is either different (i.e., the intermediates formed are different) or the slowly degrading products are easily desorbed from the surface, which enables further degradation of BPS. From this point of

view, the 1Ce1Bi sample provides much higher durability and long-term stability than P25 (and ceria), which are caused by altering the catalyst's acid−base surface properties.

Recycling Experiments. The durability of the 1Ce1Bi and P25 reactive adsorbents/photocatalysts was examined in a series of repeated MPO degradation experiments (Figure 6), with washing of the adsorbent with water and acetonitrile between cycles as described elsewhere.[25] XPS and XRD measurements were performed before and after the degradation of MPO to investigate possible structural changes of the sample 1Ce1Bi between cycles. As shown in the diffractograms of the sample before and after MPO degradation (Figure S9), no changes in the crystal structure, crystallinity, crystalline size, or any new phases resulting from MPO decomposition were detected. Similar results were obtained from XPS analysis (Figure S10, Table S10). No surface contaminants (such as P or a large amount of C) were detected, and the chemical bonding structures of Ce and Bi were not changed. Note that during the procedure, a non-negligible amount (5−10%) of the sample is lost in each cycle due to centrifugation/washing/drying and sampling from the reaction mixture. In the case of 1Ce1Bi (Figure 6a), the amount of MPO removed after two cycles (240 min each) is almost identical (<96%), and the third cycle led to a decrease in activity of about 10%, which is an excellent result taking into account material loss between cycles. This also suggests that possible MPO degradation residues are not too firmly bound to the active sites on the catalyst, and the washing procedure used may lead to catalyst regeneration. The fourth cycle leads to a higher decrease in activity (yet more than 60% of MPO was removed after 240 min), likely due to a significant loss of sorbent.

P25 (Figure 6b) can degrade up to 90.8% of the MPO in the first cycle after 240 min, but the degradation slowed rapidly after 120 min, probably due to the accumulation of intermediates that are degraded preferably. The second cycle led to a significant decrease in activity, with only 70.7% of MPO removed from the solution by adsorption/PID. In the third and, quite surprisingly, also in the fourth cycle, the removal of MPO achieved 55%. Again, no p-NP production was observed on P25, suggesting that it is either tightly bound to the surface, where it may prevent further adsorption of MPO and thus worsen its degradation in the second and subsequent cycles, or alternatively, MPO may be degraded by a different degradation pathway on P25 due to its very different surface properties compared to the 1Ce1Bi sample.

Evaluation of Toxicity In Vivo/In Vitro. The effect of pure ceria and the 1Ce1Bi sample on aquatic and other organisms was evaluated using representatives of bacteria, algae, invertebrates, and fish (Figure 7, Table S11). Concentration−response curves are presented in Figures S11−S16 in Supporting Information. The toxicity of both materials was low or even undetectable for all tested organisms. Growth inhibition did not exceed 50% even at the highest concentration tested, which made it impossible to accurately calculate EC_{50} values, which, however, were always below the limit (100 mg/L) for considering the material to be toxic to aquatic organisms. At lower nanoceria concentrations, the tested bacteria and algae even showed a slight improvement in their growth (see Supporting Information), a form of hormesis.

In Vitro rMSC PrestoBlue Cytotoxicity Assay. To assess mammalian toxicity, rMSC cells were exposed to 1Ce0Bi and 1Ce1Bi at 6 concentrations (0.001, 0.01, 0.1, 1, 10, and 100 μM) for 96 h. No significant decrease in cell viability (Figure

7h) was observed compared to the negative control (sample-free media). 1Ce0Bi and 1Ce1Bi show no significant cytotoxic effect on cultured rMSC cells.

In Vivo Toxicity Tests on Model Fish. The in vivo toxicity of pure ceria (1Ce0Bi) and the 1Ce1Bi sample was tested in the concentration range 0.001−100 μM (Figure 7a,b). Toxic effects were more severe at higher concentrations and longer exposures; however, both compounds show relatively low in vivo toxicity. Exposure to the maximum test concentration (100 μM) of 1Ce1Bi was not sufficient to induce 100% lethality. The observed morphological effects for 1Ce1Bi (Figure S17) were represented mainly by embryo coagulation, for pure ceria by coagulation, and partly by growth retardation and malformation (Figure 7c). Malformations usually indicate a possible toxic impact on the early development of zebrafish embryos. High concentrations of both compounds seem to disrupt the gastrulation process, leading to organogenesis and coagulation failure. The hatching success of the tested embryos (data not shown) did not differ significantly compared to the embryos treated with the negative control, indicating that the properties of chorion were not altered in the presence of pure ceria or 1Ce1Bi.

The LD$_{50}$ values for the 96 h time point were 5.526 μM (p = 0.001) for 1Ce0Bi and 25.757 μM (p = 0.003) for 1Ce1Bi. 1Ce1Bi shows a slightly lower toxicity compared to pure ceria, which is consistent with the very low toxicity of bismuth[29] among other heavy metals. However, as all tests show, the toxicity of prepared nanoceria and Bi-modified nanoceria is generally very low, making them a promising material for the safe use as bifunctional reactive nanoadsorbents/photocatalysts for abatement of toxic chemicals in aquatic environments.

CONCLUSIONS

Nanocrystalline cerium−bismuth oxides/oxynitrates were prepared by an easily scalable low-temperature ambient pressure method using water as the sole solvent. Photocatalytic Bi-doped nanoceria was formed up to a 1:1 molar ratio, while at higher Bi doping levels, basic bismuth oxynitrate photocatalysts with a pronounced layered structure formed nanocomposites with nanoceria. Bi doping of nanoceria induced defect formation and higher Lewis and Brønsted acidity, decreased band gap energy, increased zeta potential, and improved particle stability in solution at higher pH values, which result in higher photocatalytic activity toward OP compounds and improved adsorption and photodecomposition of bisphenols.

Bi doping enhanced the photodecomposition of the parent OP compound, but importantly it also led to efficient photodegradation of the resulting products (concretely p-NP). Bi doping also improved the adsorption/photodegradation of BPA and BPS (at prolonged times) probably due to a different degradation mechanism or efficient desorption of the reaction intermediates, leading to higher durability and long-term stability compared to P25 (and pure nanoceria).

Finally, low toxicity to mammalian cells and aquatic organisms of prepared Bi-doped nanoceria was demonstrated by comprehensive in vivo/in vitro testing on cells, bacteria, algae, invertebrates, and fish. The high activity, durability, and low toxicity of Bi-doped ceria, which acts as a bifunctional reactive nanoadsorbent/photocatalyst, make it promising for safe use in abatement of toxic chemicals in the aquatic environment.

ASSOCIATED CONTENT

Ⓢ Supporting Information

The Supporting Information is available free of charge at https://pubs.acs.org/doi/10.1021/acsanm.2c03926.

Detailed procedures for sample synthesis, characterization methods, pollutant degradation and in vivo/in vitro toxicity testing, TEM/EDS and XPS analysis of selected samples, Tauc plots and zeta potential measurements for all prepared samples, degradation kinetics for adsorption and PID of p-NP on prepared samples, material characteristics, and fitting parameters of the kinetic model for the degradation of OP compounds MPO, BNPP, and bisphenols A and S on prepared samples (PDF)

AUTHOR INFORMATION

Corresponding Author

Jiří Henych − *Institute of Inorganic Chemistry of the Czech Academy of Sciences, 250 68 Husinec-Řež, Czech Republic; Faculty of Environment, Jan Evangelista Purkyně University in Ústí nad Labem, 400 96 Ústí nad Labem, Czech Republic;* ⊙ orcid.org/0000-0002-5509-2139; Email: henych@iic.cas.cz

Authors

Martin Šťastný − *Institute of Inorganic Chemistry of the Czech Academy of Sciences, 250 68 Husinec-Řež, Czech Republic*

Zuzana Němečková − *Institute of Inorganic Chemistry of the Czech Academy of Sciences, 250 68 Husinec-Řež, Czech Republic*

Martin Kormunda − *Faculty of Science, Jan Evangelista Purkyně University in Ústí nad Labem, 400 96 Ústí nad Labem, Czech Republic*

Zuzana Šanderová − *Faculty of Science, Jan Evangelista Purkyně University in Ústí nad Labem, 400 96 Ústí nad Labem, Czech Republic*

Zuzana Žmudová − *Faculty of Science, Jan Evangelista Purkyně University in Ústí nad Labem, 400 96 Ústí nad Labem, Czech Republic*

Petr Ryšánek − *Faculty of Science, Jan Evangelista Purkyně University in Ústí nad Labem, 400 96 Ústí nad Labem, Czech Republic*

Štěpán Stehlík − *Institute of Physics of the Czech Academy of Sciences, 162 00 Prague, Czech Republic; New Technologies−Research Centre, University of West Bohemia, 306 14 Pilsen, Czech Republic;* ⊙ orcid.org/0000-0002-7212-5959

Jakub Ederer − *Faculty of Environment, Jan Evangelista Purkyně University in Ústí nad Labem, 400 96 Ústí nad Labem, Czech Republic*

Michaela Liegertová − *Faculty of Science, Jan Evangelista Purkyně University in Ústí nad Labem, 400 96 Ústí nad Labem, Czech Republic*

Josef Trögl − *Faculty of Environment, Jan Evangelista Purkyně University in Ústí nad Labem, 400 96 Ústí nad Labem, Czech Republic*

Pavel Janoš − *Faculty of Environment, Jan Evangelista Purkyně University in Ústí nad Labem, 400 96 Ústí nad Labem, Czech Republic;* ⊙ orcid.org/0000-0002-3098-4333

Complete contact information is available at:

https://pubs.acs.org/10.1021/acsanm.2c03926

Notes

The authors declare no competing financial interest.

■ REFERENCES

(1) Adeleye, A. S.; Conway, J. R.; Garner, K.; Huang, Y.; Su, Y.; Keller, A. A. Engineered Nanomaterials for Water Treatment and Remediation: Costs, Benefits, and Applicability. *Chem. Eng. J.* **2016**, *286*, 640−662.

(2) Richardson, S. D.; Kimura, S. Y. Emerging Environmental Contaminants: Challenges Facing Our next Generation and Potential Engineering Solutions. *Environ. Technol. Innovation* **2017**, *8*, 40−56.

(3) Dulio, V.; van Bavel, B.; Brorström-Lundén, E.; Harmsen, J.; Hollender, J.; Schlabach, M.; Slobodnik, J.; Thomas, K.; Koschorreck, J. Emerging Pollutants in the EU: 10 Years of NORMAN in Support of Environmental Policies and Regulations. *Environ. Sci. Eur.* **2018**, *30*, 5.

(4) Diamond, J. M.; Latimer, H. A.; Munkittrick, K. R.; Thornton, K. W.; Bartell, S. M.; Kidd, K. A. Prioritizing Contaminants of Emerging Concern for Ecological Screening Assessments. *Environ. Toxicol. Chem.* **2011**, *30*, 2385−2394.

(5) Wang, L.; Shi, C.; Wang, L.; Pan, X.; Zhang, J. J.; Zou, J.-J. Rational Design, Synthesis, Adsorption Principles and Applications of Metal Oxide Adsorbents: A Review. *Nanoscale* **2020**, *12*, 4790−4815.

(6) Aguilar-Pérez, K. M.; Avilés-Castrillo, J. I.; Ruiz-Pulido, G.; Medina, D. I.; Parra-Saldivar, R.; Iqbal, H. M. N. Nanoadsorbents in Focus for the Remediation of Environmentally-Related Contaminants with Rising Toxicity Concerns. *Sci. Total Environ.* **2021**, *779*, 146465.

(7) Medhi, R.; Marquez, M. D.; Lee, T. R. Visible-Light-Active Doped Metal Oxide Nanoparticles: Review of Their Synthesis, Properties, and Applications. *ACS Appl. Nano Mater.* **2020**, *3*, 6156−6185.

(8) Luo, J.; Fu, K.; Yu, D.; Hristovski, K. D.; Westerhoff, P.; Crittenden, J. C. Review of Advances in Engineering Nanomaterial Adsorbents for Metal Removal and Recovery from Water: Synthesis and Microstructure Impacts. *ACS ES&T Engg* **2021**, *1*, 623−661.

(9) Guan, X.; Du, J.; Meng, X.; Sun, Y.; Sun, B.; Hu, Q. Application of Titanium Dioxide in Arsenic Removal from Water: A Review. *J. Hazard. Mater.* **2012**, *215−216*, 1−16.

(10) Nagpal, M.; Kakkar, R. Use of Metal Oxides for the Adsorptive Removal of Toxic Organic Pollutants. *Sep. Purif. Technol.* **2019**, *211*, 522−539.

(11) Naseem, T.; Durrani, T. The Role of Some Important Metal Oxide Nanoparticles for Wastewater and Antibacterial Applications: A Review. *Environ. Chem. Ecotoxicol.* **2021**, *3*, 59−75.

(12) Mazurkow, J. M.; Yüzbasi, N. S.; Domagala, K. W.; Pfeiffer, S.; Kata, D.; Graule, T. Nano-Sized Copper (Oxide) on Alumina Granules for Water Filtration: Effect of Copper Oxidation State on Virus Removal Performance. *Environ. Sci. Technol.* **2020**, *54*, 1214−1222.

(13) Sharma, R. K.; Solanki, K.; Dixit, R.; Sharma, S.; Dutta, S. Nanoengineered Iron Oxide-Based Sorbents for Separation of Various Water Pollutants: Current Status, Opportunities and Future Outlook. *Environ. Sci.: Water Res. Technol.* **2021**, *7*, 818−860.

(14) Zeng, H.; Yin, C.; Qiao, T.; Yu, Y.; Zhang, J.; Li, D. As(V) Removal from Water Using a Novel Magnetic Particle Adsorbent Prepared with Iron-Containing Water Treatment Residuals. *ACS Sustainable Chem. Eng.* **2018**, *6*, 14734−14742.

(15) Abodif, A. M.; Meng, A. M.; Ma, L.; Ahmed, S.; Belvett, A. S. A.; Wei, N.; Ning, Z. Z.; Ning, D. Mechanisms and Models of Adsorption: TiO2-Supported Biochar for Removal of 3,4-Dimethylaniline. *ACS Omega* **2020**, *5*, 13630−13640.

(16) Mustapha, S.; Tijani, J. O.; Ndamitso, M. M.; Abdulkareem, S. A.; Shuaib, D. T.; Mohammed, A. K.; Sumaila, A. The Role of Kaolin and Kaolin/ZnO Nanoadsorbents in Adsorption Studies for Tannery Wastewater Treatment. *Sci. Rep.* **2020**, *10*, 13068.

(17) Islam, M. A.; Morton, D. W.; Johnson, B. B.; Mainali, B.; Angove, M. J. Manganese Oxides and Their Application to Metal Ion and Contaminant Removal from Wastewater. *J. Water Process Eng.* **2018**, *26*, 264−280.

(18) Kim, E. J.; Lee, C. S.; Chang, Y. Y.; Chang, Y. S. Hierarchically Structured Manganese Oxide-Coated Magnetic Nanocomposites for the Efficient Removal of Heavy Metal Ions from Aqueous Systems. *ACS Appl. Mater. Interfaces* **2013**, *5*, 9628−9634.

(19) Clark, A. H.; Beyer, K. A.; Hayama, S.; Hyde, T. I.; Sankar, G. Unusual Redox Behavior of Ceria and Its Interaction with Hydrogen. *Chem. Mater.* **2019**, *31*, 7744−7751.

(20) Montini, T.; Melchionna, M.; Monai, M.; Fornasiero, P. Fundamentals and Catalytic Applications of CeO2-Based Materials. *Chem. Rev.* **2016**, *116*, 5987−6041.

(21) Xu, C.; Qu, X. Cerium Oxide Nanoparticle: A Remarkably Versatile Rare Earth Nanomaterial for Biological Applications. *NPG Asia Mater.* **2014**, *6*, No. e90.

(22) Khulbe, K.; Karmakar, K.; Ghosh, S.; Chandra, K.; Chakravortty, D.; Mugesh, G. Nanoceria-Based Phospholipase-Mimetic Cell Membrane Disruptive Antibiofilm Agents. *ACS Appl. Bio Mater.* **2020**, *3*, 4316−4328.

(23) Janos, P.; Kuran, P.; Kormunda, M.; Stengl, V.; Grygar, T. M.; Dosek, M.; Stastny, M.; Ederer, J.; Pilarova, V.; Vrtoch, L. Cerium Dioxide as a New Reactive Sorbent for Fast Degradation of Parathion Methyl and Some Other Organophosphates. *J. Rare Earths* **2014**, *32*, 360−370.

(24) Janoš, P.; Henych, J.; Pelant, O.; Pilařová, V.; Vrtoch, L.; Kormunda, M.; Mazanec, K.; Štengl, V. Cerium Oxide for the Destruction of Chemical Warfare Agents: A Comparison of Synthetic Routes. *J. Hazard. Mater.* **2016**, *304*, 259−268.

(25) Henych, J.; Šťastný, M.; Němečková, Z.; Mazanec, K.; Tolasz, J.; Kormunda, M.; Ederer, J.; Janoš, P. Bifunctional TiO2/CeO2 Reactive Adsorbent/Photocatalyst for Degradation of Bis-p-Nitrophenyl Phosphate and CWAs. *Chem. Eng. J.* **2021**, *414*, 128822.

(26) Henych, J.; Janoš, P.; Kormunda, M.; Tolasz, J.; Štengl, V. Reactive Adsorption of Toxic Organophosphates Parathion Methyl and DMMP on Nanostructured Ti/Ce Oxides and Their Composites. *Arabian J. Chem.* **2019**, *12*, 4258−4269.

(27) Mullins, D. R. The Surface Chemistry of Cerium Oxide. *Surf. Sci. Rep.* **2015**, *70*, 42−85.

(28) Paier, J.; Penschke, C.; Sauer, J. Oxygen Defects and Surface Chemistry of Ceria: Quantum Chemical Studies Compared to Experiment. *Chem. Rev.* **2013**, *113*, 3949−3985.

(29) Wang, R.; Li, H.; Sun, H. *Bismuth: Environmental Pollution and Health Effects.* Encyclopedia of Environmental Health, 2019; pp 415−423.

(30) Wang, Y.; Xie, Y.; Zhang, C.; Chen, W.; Wang, J.; Zhang, R.; Yang, H. Tuning the Oxygen Mobility of CeO2 via Bi-Doping for

Diesel Soot Oxidation: Experimental and DFT Studies. *J. Environ. Chem. Eng.* **2021**, *9*, 105049.

(31) Cui, B.; Li, Y.; Li, S.; Xia, Y.; Zheng, Z.; Liu, Y. Q. Bi-Doped Ceria as a Highly Efficient Catalyst for Soot Combustion: Improved Mobility of Lattice Oxygen in CexBi1-xOy Catalysts. *Energy Fuels* **2020**, *34*, 9932−9939.

(32) Yu, K.; Lei, D.; Feng, Y.; Yu, H.; Chang, Y.; Wang, Y.; Liu, Y.; Wang, G. C.; Lou, L. L.; Liu, S.; Zhou, W. The role of Bi-doping in promoting electron transfer and catalytic performance of Pt/3DOM-Ce1−Bi O2−δ. *J. Catal.* **2018**, *365*, 292−302.

(33) Sardar, K.; Playford, H. Y.; Darton, R. J.; Barney, E. R.; Hannon, A. C.; Tompsett, D.; Fisher, J.; Kashtiban, R. J.; Sloan, J.; Ramos, S.; Cibin, G.; Walton, R. I. Nanocrystalline Cerium−Bismuth Oxides: Synthesis, Structural Characterization, and Redox Properties. *Chem. Mater.* **2010**, *22*, 6191−6201.

(34) Veedu, S. N.; Jose, S.; Narendranath, S. B.; Prathapachandra Kurup, M. R.; Periyat, P. Visible Light-Driven Photocatalytic Degradation of Methylene Blue Dye over Bismuth-Doped Cerium Oxide Mesoporous Nanoparticles. *Environ. Sci. Pollut. Res.* **2021**, *28*, 4147−4155.

(35) Santra, C.; Auroux, A.; Chowdhury, B. Bi Doped CeO2 Oxide Supported Gold Nanoparticle Catalysts for the Aerobic Oxidation of Alcohols. *RSC Adv.* **2016**, *6*, 45330−45342.

(36) Henych, J.; Šťastný, M.; Ederer, J.; Němečková, Z.; Pogorzelska, A.; Tolasz, J.; Kormunda, M.; Ryšánek, P.; Bażanów, B.; Stygar, D.; Mazanec, K.; Janoš, P. How the Surface Chemical Properties of Nanoceria Are Related to Its Enzyme-like, Antiviral and Degradation Activity. *Environ. Sci.: Nano* **2022**, *9*, 3485−3501.

(37) Trögl, J.; Benediktová, K. Empirical Comparison of Seven Two-Parameter Sigmoid Equations for the Evaluation of the Concentration-Response Curves from Standard Acute Ecotoxicity Assays. *Int. J. Environ. Res.* **2011**, *5*, 989−998.

(38) Panuška, P.; Nejedlá, Z.; Smejkal, J.; Aubrecht, P.; Liegertová, M.; Štofik, M.; Havlica, J.; Malý, J. A Millifluidic Chip for Cultivation of Fish Embryos and Toxicity Testing Fabricated by 3D Printing Technology. *RSC Adv.* **2021**, *11*, 20507−20518.

(39) Frolova, Y. V.; Kochubey, D. I.; Kriventsov, V. V.; Moroz, E. M.; Neofitides, S.; Sadykov, V. A.; Zyuzin, D. A. The Influence of Bismuth Addition on the Local Structure of CeO2. *Nucl. Instrum. Methods Phys. Res., Sect. A* **2005**, *543*, 127−130.

(40) Prekajski, M.; Dohčević-Mitrović, Z.; Radović, M.; Babić, B.; Pantić, J.; Kremenović, A.; Matović, B. Nanocrystaline solid solution CeO2-Bi2O3. *J. Eur. Ceram. Soc.* **2012**, *32*, 1983−1987.

(41) Mavuso, M. A.; Makgwane, P. R.; Ray, S. S. Heterostructured CeO2-M (M = Co, Cu, Mn, Fe, Ni) Oxide Nanocatalysts for the Visible-Light Photooxidation of Pinene to Aroma Oxygenates. *ACS Omega* **2020**, *5*, 9775−9788.

(42) Fronzi, M.; Piccinin, S.; Delley, B.; Traversa, E.; Stampfl, C. Water Adsorption on the Stoichiometric and Reduced CeO2(111) Surface: A First-Principles Investigation. *Phys. Chem. Chem. Phys.* **2009**, *11*, 9188−9199.

(43) Vincent, A.; Inerbaev, T. M.; Babu, S.; Karakoti, A. S.; Self, W. T.; Masunov, A. E.; Seal, S. Tuning Hydrated Nanoceria Surfaces: Experimental/Theoretical Investigations of Ion Exchange and Implications in Organic and Inorganic Interactions. *Langmuir* **2010**, *26*, 7188−7198.

(44) Christensen, A. N.; Chevallier, M. A.; Skibsted, J.; Iversen, B. B. Synthesis and Characterization of Basic Bismuth(III) Nitrates. *J. Chem. Soc., Dalton Trans.* **2000**, *3*, 265−270.

(45) Han, Q.; Pang, J.; Wang, X.; Wu, X.; Zhu, J. Synthesis of Unique Flowerlike Bi2O2(OH)(NO3) Hierarchical Microstructures with High Surface Area and Superior Photocatalytic Performance. *Chem.—Eur. J.* **2017**, *23*, 3891−3897.

(46) Yang, L. M.; Zhang, G. Y.; Liu, Y.; Xu, Y. Y.; Liu, C. M.; Liu, J. W. A {110} facet predominated Bi6O6(OH)3(NO3)3·1.5H2O photocatalyst: selective hydrothermal synthesis and its superior photocatalytic activity for degradation of phenol. *RSC Adv.* **2015**, *5*, 79715−79723.

(47) Lu, B.; Zhu, Y. Synthesis and Photocatalysis Performances of Bismuth Oxynitrate Photocatalysts with Layered Structures. *Phys. Chem. Chem. Phys.* **2014**, *16*, 16509−16514.

(48) Sun, S.; Xiao, W.; You, C.; Zhou, W.; Garba, Z. N.; Wang, L.; Yuan, Z. Methods for Preparing and Enhancing Photocatalytic Activity of Basic Bismuth Nitrate. *J. Clean. Prod.* **2021**, *294*, 126350.

(49) Henry, N.; Evain, M.; Deniard, P.; Jobic, S.; Mentré, O.; Abraham, F. [Bi6O4.5(OH)3.5]2(NO3)11: a new anhydrous bismuth basic nitrate. Synthesis and structure determination from twinned crystals. *J. Solid State Chem.* **2003**, *176*, 127−136.

(50) Denisov, V. N.; Ivlev, A. N.; Lipin, A. S.; Mavrin, B. N.; Orlov, V. G. Raman spectra and lattice dynamics of single-crystal. *J. Phys.: Condens. Matter* **1997**, *9*, 4967−4978.

(51) Malligavathy, M.; Pathinettam Padiyan, D. Role of PH in the Hydrothermal Synthesis of Phase Pure Alpha Bi2O3 Nanoparticles and Its Structural Characterization. *Adv. Mater. Processes* **2021**, *2*, 51−55.

(52) Ho, C.-H.; Chan, C.-H.; Huang, Y.-S.; Tien, L.-C.; Chao, L.-C. The study of optical band edge property of bismuth oxide nanowires α-Bi_2O_3. *Opt. Express* **2013**, *21*, 11965.

(53) Pye, C. C.; Gunasekara, C. M.; Rudolph, W. W. An Ab Initio Investigation of Bismuth Hydration. *Can. J. Chem.* **2007**, *85*, 945−950.

(54) Pang, J.; Han, Q.; Liu, W.; Shen, Z.; Wang, X.; Zhu, J. Two basic bismuth nitrates: [Bi6O6(OH)2](NO3)4· 2H2O with superior photodegradation activity for rhodamine B and [Bi6O5(OH)3]-(NO3)5· 3H2O with ultrahigh adsorption capacity for methyl orange. *Appl. Surf. Sci.* **2017**, *422*, 283−294.

(55) Frost, R. L.; Čejka, J.; Sejkora, J.; Plášil, J.; Reddy, B. J.; Keeffe, E. C. Raman Spectroscopic Study of a Hydroxy-Arsenate Mineral Containing Bismuth-Atelestite Bi2O(OH)(AsO4). *Spectrochim. Acta, Part A* **2011**, *78*, 494−496.

(56) Fruth, V.; Popa, M.; Berger, D.; Ionica, C. M.; Jitianu, M. Phases Investigation in the Antimony Doped Bi2O3 System. *J. Eur. Ceram. Soc.* **2004**, *24*, 1295−1299.

(57) Ziegler, P.; Grigoraviciute, I.; Gibson, K.; Glaser, J.; Kareiva, A.; Meyer, H. J. On the characterization of BiMO2NO3 (M=Pb, Ca, Sr, Ba) materials related with the Sillén X1 structure. *J. Solid State Chem.* **2004**, *177*, 3610−3615.

(58) Henry, N.; Evain, M.; Deniard, P.; Jobic, S.; Abraham, F.; Mentré, O. [Bi2O2]2+ Layers in Bi2O2(OH)(NO3): Synthesis And Structure Determination. *Z. Naturforsch., B: J. Chem. Sci.* **2005**, *60*, 322−327.

(59) Cheng, H.; Huang, B.; Lu, J.; Wang, Z.; Xu, B.; Qin, X.; Zhang, X.; Dai, Y. Synergistic Effect of Crystal and Electronic Structures on the Visible-Light-Driven Photocatalytic Performances of Bi2O3 Polymorphs. *Phys. Chem. Chem. Phys.* **2010**, *12*, 15468−15475.

(60) Maslakov, K. I.; Teterin, Y. A.; Popel, A. J.; Teterin, A. Y.; Ivanov, K. E.; Kalmykov, S. N.; Petrov, V. G.; Petrov, P. K.; Farnan, I. XPS study of ion irradiated and unirradiated CeO2 bulk and thin film samples. *Appl. Surf. Sci.* **2018**, *448*, 154−162.

(61) Šťastný, M.; Issa, G.; Popelková, D.; Ederer, J.; Kormunda, M.; Kříženecká, S.; Henych, J. Nanostructured Manganese Oxides as Highly Active Catalysts for Enhanced Hydrolysis of Bis(4-Nitrophenyl)Phosphate and Catalytic Decomposition of Methanol. *Catal. Sci. Technol.* **2021**, *11*, 1766−1779.

(62) Zaki, M. I.; Hasan, M. A.; Al-Sagheer, F. A.; Pasupulety, L. In Situ FTIR Spectra of Pyridine Adsorbed on SiO2-Al2O3, TiO2, ZrO2 and CeO2: General Considerations for the Identification of Acid Sites on Surfaces of Finely Divided Metal Oxides. *Colloids Surf., A* **2001**, *190*, 261−274.

(63) Zaki, M. I.; Hussein, G. A. M.; Mansour, S. A. A.; El-Ammawy, H. A. Adsorption and Surface Reactions of Pyridine on Pure and Doped Ceria Catalysts as Studied by Infrared Spectroscopy. *J. Mol. Catal.* **1989**, *51*, 209−220.

(64) Marsh, J. L.; Wayman, A. E.; Smiddy, N. M.; Campbell, D. J.; Parker, J. C.; Bosma, W. B.; Remsen, E. E. Infrared Spectroscopic Analysis of the Adsorption of Pyridine Carboxylic Acids on Colloidal Ceria. *Langmuir* **2017**, *33*, 13224−13233.

(65) Wilson, C.; Cooper, N. J.; Briggs, M. E.; Cooper, A. I.; Adams, D. J. Investigating the Breakdown of the Nerve Agent Simulant Methyl Paraoxon and Chemical Warfare Agents GB and VX Using Nitrogen Containing Bases. *Org. Biomol. Chem.* **2018**, *16*, 9285−9291.

(66) Ragunathan, K. G.; Schneider, H. J. Binuclear Lanthanide Complexes as Catalysts for the Hydrolysis of Bis(p-Nitrophenyl)-Phosphate and Double-Stranded DNA. *Angew. Chem., Int. Ed. Engl.* **1996**, *35*, 1219−1221.

(67) Masula, K.; Bhongiri, Y.; Raghav Rao, G.; Vijay Kumar, P.; Pola, S.; Basude, M. Evolution of photocatalytic activity of CeO2-Bi2O3 composite material for wastewater degradation under visible-light irradiation. *Opt. Mater.* **2022**, *126*, 112201.

(68) López-Ramón, M. V.; Ocampo-Pérez, R.; Bautista-Toledo, M. I.; Rivera-Utrilla, J.; Moreno-Castilla, C.; Sánchez-Polo, M. Removal of Bisphenols A and S by Adsorption on Activated Carbon Clothes Enhanced by the Presence of Bacteria. *Sci. Total Environ.* **2019**, *669*, 767−776.